



CFD simulation of floating body motion with mooring dynamics: Coupling MoorDyn with OpenFOAM

Haifei Chen^{a,*}, Matthew Hall^b

^a Interdisciplinary Science Cooperative, University of New Mexico, Albuquerque, NM 87131, USA

^b National Renewable Energy Laboratory, Golden, CO 80401, USA



ARTICLE INFO

Keywords:

Floating body
Waves
OpenFOAM
Overset
Mooring dynamics
MoorDyn
Fluid-structure interaction

ABSTRACT

It is increasingly popular to use Computational Fluid Dynamics (CFD) models to study floating structures subjected to ocean waves, especially when it comes to applications of floating offshore wind turbines and Wave Energy Converters (WECs). Mooring dynamics are currently lacking in most of these applications. This paper presents a coupled simulation study of moored floating body motion by coupling two open-source libraries: a finite volume CFD toolbox, OpenFOAM, and a lumped-mass mooring model, MoorDyn. The instantaneous floating body position and velocity are passed from the body motion solver in the CFD model to the mooring model to calculate the fairlead kinematics. The mooring reaction forces, which are calculated by MoorDyn after updating the mooring system states, are then returned to the body motion solver to update the floating body motion. Both mesh deformation and overset mesh methods are used as the mesh motion solver in the CFD model to account for the floating body motion. The coupled model was validated against experimental measurements for a floating box moored with four catenary lines under the action of regular waves, which came from a preliminary test campaign for WECs. Apart from the lumped-mass mooring model, the present work also coupled a quasi-static mooring model and a finite element model with the floating body motion solver in OpenFOAM. The mooring line tensions predicted by these models were compared. The coupled model equipped with three mooring line codes may be further used to carry out survivability studies of FOWTs and WECs subject to severe sea states.

1. Introduction

The last several decades have seen an increasing number of Computational Fluid Dynamics (CFD) studies on the coupled dynamics of floating structures—accounting for wind, waves, currents, and mooring lines—thanks to significant advances in computing power and computational algorithms development. Advances in CFD approaches include the Volume of Fluid (VOF) scheme for capturing the free surface in mesh-based CFD methods (Hirt and Nichols, 1981; Lin and Liu, 1998), and the Smoothed Particle Hydrodynamics (SPH) in mesh-free method (Dalrymple and Rogers, 2006; Lind et al., 2020). Besides conventional offshore oil & gas floating platforms, new ocean technologies such as Floating Offshore Wind Turbines (FOWT) and Wave Energy Converters (WEC) are being developed in order to exploit the vast resources of ocean renewable energy. For floating structures, the mooring system typically provides critical restoring forces or moments in the surge, sway, and yaw degrees of freedom, for which the hydrostatic

counterparts are absent (Liu et al., 2017). One of the most common practices in CFD simulations of FOWTs has been to use a quasi-static mooring model to represent the mooring system effects. For example, a quasi-static mooring model was adopted in the coupled aero-hydrodynamic studies of FOWTs using open-source software OpenFOAM (Cheng et al., 2019; Liu et al., 2017), commercial software STAR-CCM+ (Tran and Kim, 2016, 2018; Zhang and Kim, 2018), and ship hydrodynamics code CFDShip-Iowa (Quallen et al., 2014). All these software are well established mesh-based CFD packages for which variable-resolution grid generation and a range of turbulence models are easily accessible. In comparison, there were few mesh-free CFD studies on FOWTs coupled with mooring systems (Lyu et al., 2022). The Lagrangian meshless (particle) methods such as SPH are ideal tools to simulate free surface flows and violent wave-structure interactions since no special treatment is needed to capture the free surface in contrast with mesh-based methods. One great attraction of the particle methods is that some SPH implementations on Graphics Computing Units (GPUs)

* Corresponding author at: The University of New Mexico, Albuquerque, NM 87106, United States.

E-mail address: hfchen@unm.edu (H. Chen).

can accelerate the simulation speed by up to two orders of magnitude compared to the performance of the equivalent CPU version, making the power of mini-supercomputers more accessible (Lind et al., 2020). However, there are some challenges that may hinder widespread use of particle methods, such as adaptive particle refinement and turbulence modeling (Lind et al., 2020; Luo et al., 2021).

While quasi-static mooring models can predict floating body responses with reasonable accuracy (under mild environmental conditions), they tend to severely underestimate mooring line tensions (Hall et al., 2014; Hall and Goupee, 2015; Liu et al., 2017; Masciola et al., 2013). For survivability studies of ocean devices harnessing wind or wave energy, it is desirable to have a high-fidelity model that can resolve the coupled dynamics of the floating structure and its mooring system under combined wind, wave, and current loads. Chen et al. (2018) developed a finite difference dynamic mooring model considering current loads and studied the impact of nonlinear mooring dynamics on a spar type FOWT in the presence of current. Their results showed that current loads could have a considerable impact on the restoring effect of the mooring system and hence the FOWT response. As a matter of fact, mooring dynamics are currently lacking in most previous CFD studies (e.g., Bruinsma et al., 2018; Martin et al., 2020). Increasing efforts are being made to incorporate mooring dynamics codes into CFD studies of floating structures. Huang and Chen (2021) coupled the Finite-Analytic Navier-Stokes (FANS) CFD code with an in-house mooring analysis program, MOORING3D, to study the dynamic responses of a catenary anchor leg mooring buoy system in waves. Palm et al. (2016) presented a coupled CFD-mooring analysis for floating WECs without power take-off and validated the model with experiments of a cylindrical buoy in regular waves. The coupling was implemented between the native rigid body motion solver of OpenFOAM and an in-house mooring code, Moody.

There are unique challenges with designing mooring systems for floating WECs, which need to be installed in unsheltered and relatively shallow waters with large wave energy density (Johanning et al., 2007; Xu et al., 2019). The effects of waves, tides, and currents on WECs can be of greater concern than for other deeper water floating structures. The station-keeping functionality of the mooring system may restrain the WEC motion, which then affects energy conversion efficiency.

The aim of this paper is to incorporate a mooring dynamics model, MoorDyn, into the popular CFD toolbox, OpenFOAM, both of which are open source and thus are widely accessible to the research community and industry practitioners. MoorDyn is a lumped-mass dynamic mooring line model that was designed for coupling with other numerical models of floating body motions (Hall and Goupee, 2015). It is currently under active development, with cable bending stiffness and wave kinematics being added to the model (Hall, 2020; Hall et al., 2021). MoorDyn

mooring model was recently coupled with the SPH code DualSPHysics to simulate floating structures with catenary and taut moorings (Domínguez et al., 2019; Liu and Wang, 2020).

OpenFOAM is a leading open-source software for Computational Fluid Dynamics (Weller et al., 1998). It is written in C++ and has a modular code structure that allows users to develop customized numerical solvers as well as pre- and post-processing utilities. For free-surface Newtonian flows, OpenFOAM contains a standard solver, *interFoam*, for solving the Navier-Stokes equations for two incompressible phases. Two community contributions on numerical wavemakers (Higuera et al., 2013; Jacobsen et al., 2012), both of which were developed on top of this solver, have made OpenFOAM widely used for simulating free surface flows in coastal and ocean engineering applications. It has been demonstrated that the *interFoam* free surface flow solver coupled with the native body motion solver in OpenFOAM is capable of simulating wave-induced motions of floating objects (e.g., Palm et al., 2016; Bruinsma et al., 2018; Chen et al., 2018). Recently, Lee et al. (2021) and Tsai et al. (2021) coupled a dynamic mooring model with this flow solver and studied motions of a moored floating structure in regular waves. Both studies used mesh deformation (mesh morphing) technique to accommodate the floating body motion, and the coupling efforts entailed customizing and recompiling the flow solver. Instead, in the present paper the coupling is achieved by creating a new rigid body restraint, *sixDoFRigidBodyMotionRestraint*, which is compiled into a dynamic library and at run time can be simply loaded into the existing flow solvers in OpenFOAM, *interDyMFoam* and *over-InterDyMFoam*. The latter flow solver supports the overset grid method, which is particularly suitable for large-amplitude body motions. To the best of the authors' knowledge, there is currently no open-source mooring dynamics implementation for the overset grid flow solver. In addition to the lumped-mass mooring model MoorDyn, the quasi-static mooring model MAP++ and the finite element model Moody are also coupled with the body motion solver in OpenFOAM. The coupling code is open-source and publicly available.

The paper is structured as follows. Section 2 describes the various components of the coupled model, including the free surface flow solver, the floating body motion solver, mesh motion solver, the mooring dynamics model, and the coupling procedure between the mooring model and the CFD model. In Section 3, the implementation of the coupled model is validated against experimental measurements for a floating box moored with four catenary lines under the action of regular waves. Good agreements are obtained for the surface elevation, the box motion (surge, heave, pitch), and the mooring line anchor tension. The tension results by a quasi-static mooring model and a finite element model are also presented and discussed. Conclusions are drawn in Section 4.

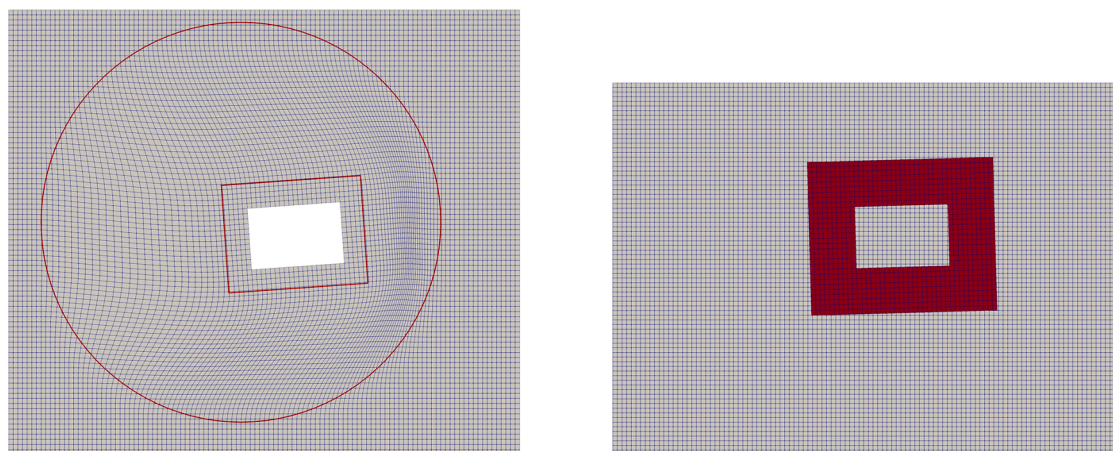


Fig. 1. Comparison of two dynamic mesh motion methods. Left: deforming mesh method (mesh morphing), where the region between the circle and the rectangle delimits the scope of deformed cells. Right: overset mesh method, in which the overset grid (in red) lies on top of and moves relative to the background mesh.

Table 1

Main features of three mooring line analysis codes.

Code	MoorDyn	MAP++	Moody
Analysis type	Dynamic	Quasi-static	Dynamic
Model basis	Lumped-mass	Catenary equation	Finite element
Integration	Second-order Runge-Kutta	N/A	Third-order Runge-Kutta
Programming language	C++, Fortran • Wrapper in C++, Fortran, Python, MATLAB	C • Wrapper in C, C++, Fortran, Python	C+ • Wrapper in C++, Fortran, MATLAB
Main features	Includes axial stiffness and internal damping forces, bending stiffness, line weight, buoyancy, seabed contact, and drag and inertia forces (Morison's equation) • Fluid forces (current and waves) on lines are being implemented • Supports arbitrary line interconnections, clump weights and floats, submerged rigid bodies • Ignores torsion	Includes axial elasticity, line weight, buoyancy, and seabed contact • Supports arbitrary line interconnections, clump weights and floats • Ignores bending, torsion, and current and wave forces (drag & inertia)	Includes axial stiffness and internal damping forces, line weight, buoyancy, seabed contact, and drag and inertia forces (Morison's equation) • Includes current and wave forces on lines • Supports submerged rigid bodies (modeled as points and cylinders) • Ignores bending and torsion
Source code	https://github.com/mattEhall/MoorDyn	https://bitbucket.org/mmasciola/map-plus-plus	Precompiled library
Documentation	https://moordyn.readthedocs.io/en/latest	https://map-plus-plus.readthedocs.io/en/latest	https://github.com/johannep/moodyAPI
Reference	Hall and Goupee (2015); Hall (2020); Hall et al. (2021)	Mascioli et al. (2013)	Palm et al. (2016, 2017)

2. Methodology

The present study adopts the open-source CFD toolbox OpenFOAM as the CFD model, and it mainly uses MoorDyn as the mooring dynamics model. To simulate the floating body motion within a reasonable amount of time, Reynolds-Averaged Navier-Stokes (RANS) equations are solved in the CFD flow solver. The various components required in the coupled CFD-mooring model are described in this section.

2.1. Free-surface flow solver

The *interFoam* solver in OpenFOAM is an air-water two-phase flow solver and is the basic free surface flow solver used in this study. It solves the RANS equations for two incompressible phases using a finite volume discretization and the Volume of Fluid (VOF) surface capturing method (Jasak, 1996; Rusche, 2002). The RANS equations describing mass continuity and conservation of momentum for an incompressible fluid are given by

$$\nabla \cdot \mathbf{U} = 0 \quad (1)$$

$$\frac{\partial \rho \mathbf{U}}{\partial t} + \nabla \cdot (\rho \mathbf{U} \mathbf{U}) - \nabla \cdot (\mu_{\text{eff}} \nabla \mathbf{U}) = -\nabla p^* - \mathbf{g} \cdot \mathbf{X} \nabla \rho + \nabla \mathbf{U} \cdot \nabla \mu_{\text{eff}} \quad (2)$$

where \mathbf{U} is the fluid velocity vector in Cartesian coordinates, ρ is the density of the mixed fluid, $p^* = p - \rho \mathbf{g} \cdot \mathbf{X}$ is the pseudo-dynamic pressure, p is the total pressure, \mathbf{g} is the acceleration due to gravity, \mathbf{X} is the position vector of the computational cells, and $\mu_{\text{eff}} = \mu + \mu_t$ is the effective dynamic viscosity, which is the sum of the molecular dynamic viscosity μ and the turbulent dynamic viscosity μ_t .

Table 2

Properties of the floating box and the mooring lines for the Esflowc experiments (Wu et al., 2019).

Properties	Value
Box length	20 cm
Box width	20 cm
Box height	13.2 cm
Box mass (with connections)	3.16 kg
Box center of gravity (x, y, z)	(0, 0, -1.26) cm
Box initial draft	7.86 cm
Box moment of inertia (I_{xx}, I_{yy}, I_{zz})	(0.015, 0.015, 0.021) kg·m ²
Mooring line diameter	3.656 mm
Mooring line mass per unit length	0.607 g/cm
Mooring line length	145.5 cm
Mooring axial stiffness	19 N

The two immiscible fluids of air and water are considered as one effective fluid and solved simultaneously throughout the computational domain, where the volume fraction of water in a computational cell, α , serves as an indicator function to mark the location of the air-water interface. The VOF function dictates that $\alpha = 1$ if the cell is full of water, $\alpha = 0$ if the cell is full of air, and $0 < \alpha < 1$ if the cell is a mixture of the two fluids. The location of the air-water interface can be approximated by taking an iso-surface of $\alpha = 0.5$ in the interface cells. The local density ρ and the local viscosity μ of the fluid ($\mu_{\text{water}} = 1.0 \times 10^{-3}$ Pa·s and $\mu_{\text{air}} = 1.48 \times 10^{-5}$ Pa·s) in each cell are weighted by

$$\rho = \alpha \rho_{\text{water}} + (1 - \alpha) \rho_{\text{air}} \quad (3)$$

$$\mu = \alpha \mu_{\text{water}} + (1 - \alpha) \mu_{\text{air}} \quad (4)$$

The VOF function is tracked by the advection equation

$$\frac{\partial \alpha}{\partial t} + \nabla \cdot (\mathbf{U} \alpha) + \nabla \cdot (\mathbf{U}_t \alpha (1 - \alpha)) = 0 \quad (5)$$

in which a third term is added to the classic VOF transport equation to limit the smearing of the interface (Hirt and Nichols, 1981). This artificial convective term is active only in a thin interface region where $0 < \alpha < 1$. More details about the VOF method can be found in Rusche (2002).

Table 3

Global coordinates of mooring line fairlead (a-d) and anchoring (A-D) connections.

Location	Coordinates x, y, z (m)
Fairlead a	-0.1, 0.1, -0.0736
Fairlead b	-0.1, -0.1, -0.0736
Fairlead c	0.1, 0.1, -0.0736
Fairlead d	0.1, -0.1, -0.0736
Anchor A	-1.385, 0.423, -0.5
Anchor B	-1.385, -0.423, -0.5
Anchor C	1.385, 0.423, -0.5
Anchor D	1.385, -0.423, -0.5

Table 4

Incident regular wave conditions for model validation.

Case #	Wave height H (m)	Wave period T (s)	Water depth h (m)	Wave length L (m)
H12T18	0.12	1.8	0.5	3.57
H12T20	0.12	2.0	0.5	4.06
H15T18	0.15	1.8	0.5	3.57

Table 5
Positions of the wave gauges within the numerical wave flume.

Wave gauges	x (m)	y (m)
WG1	-2.74	0
WG2	-0.05	0.26
WG3	0.07	-0.36
WG4	0.55	0
WG5	1.9	0
WG6	2.9	0

2.2. Floating body motions

The native rigid body motion library in OpenFOAM, i.e. *sixDoFRigidBodyMotion*, is applied to solve the six degrees of freedom (6-DoF) motion for the floating body. The equations of motion are formulated based on the conservation of linear and angular momentum:

$$\frac{d\mathbf{v}_f}{dt} = \mathbf{F}_f/m_f \quad (6)$$

$$\frac{d\boldsymbol{\omega}_f}{dt} = \mathbf{I}_f^{-1} \cdot (\mathbf{M}_f - \boldsymbol{\omega}_f \times (\mathbf{I}_f \cdot \boldsymbol{\omega}_f)) \quad (7)$$

where the subscript *f* denotes the quantities for the floating body. \mathbf{v}_f and $\boldsymbol{\omega}_f$ are the linear and angular velocity of the body, and m_f and \mathbf{I}_f are the mass and moment of inertia of the body. \mathbf{F}_f and \mathbf{M}_f are the total external forces and moments acting on the body calculated by

$$\mathbf{F}_f = \iint_s (p\mathbf{I} + \boldsymbol{\tau}) \cdot d\mathbf{S} + \mathbf{F}_{mooring} + m_f \mathbf{g} \quad (8)$$

$$\mathbf{M}_f = \iint_s \mathbf{r}_{CS} \times (p\mathbf{I} + \boldsymbol{\tau}) \cdot d\mathbf{S} + \mathbf{r}_{CM} \times \mathbf{F}_{mooring} + \mathbf{r}_{CG} \times m_f \mathbf{g} \quad (9)$$

where \mathbf{I} is the identity matrix, $\boldsymbol{\tau}$ is the viscous stress, and \mathbf{S} denotes the floating body's surface. The fluid forces on the body are calculated by integrating the normal pressure and the tangential shear stress over the body's boundary (Gatin et al., 2017). $\mathbf{F}_{mooring}$ is the mooring reaction force, while \mathbf{r}_{CS} , \mathbf{r}_{CM} and \mathbf{r}_{CG} are the moment arms of the hydrodynamic force, mooring force and gravity force, respectively. When the center of mass and center of rotation are identical, $\mathbf{r}_{CG} = 0$. Based on the linear and angular accelerations from Eq. (8) and Eq. (9), the Newmark integration scheme is applied to update the velocity, position, and orientation of the floating body.

2.3. Dynamic mesh motion

Two mesh motion methods are applied in this study to accommodate the floating body motion in the CFD computational domain (see Fig. 1 for a demonstration). The first method is the mesh deformation or mesh morphing technique, which is the classical method to accommodate body motion in the computational domain without topological changes (Jasak and Tukovc, 2010). Note that this mesh deformation method is suitable for small amplitude body motions, as large motions (translation or rotation) may continuously squeeze and stretch the computational cells, resulting in deteriorated mesh quality (such as large aspect ratio cells or highly skewed and severely non-orthogonal cell faces) and thus adversely affect simulation results. Jacobsen et al. (2012) found that it is

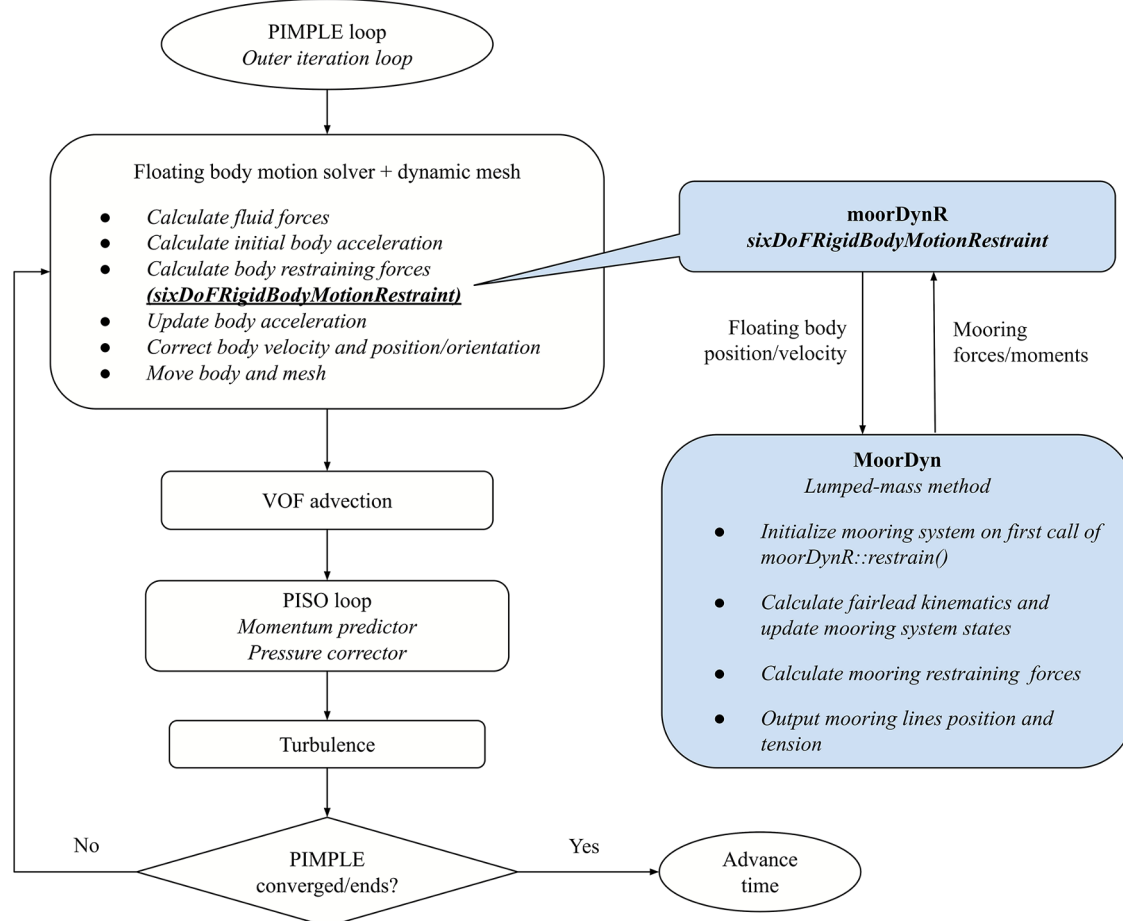


Fig. 2. Flowchart of a coupled CFD simulation (within a single time step) of floating body motion with mooring dynamics model MoorDyn incorporated in OpenFOAM's two-phase flow solver.

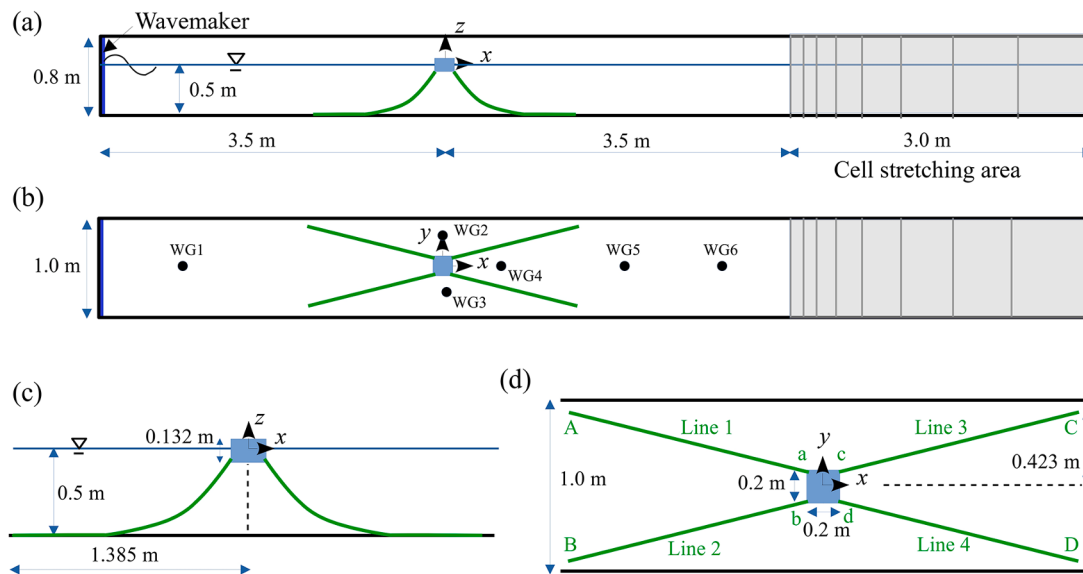


Fig. 3. Numerical model setup for the physical experiment (Wu et al., 2019). (a) Side view and (b) plan view of the numerical wave flume. (c) Side view and (d) plan view of the detailed configuration of the floating box and the 4-point symmetric catenary mooring system. The vertical domain size is 0.8 m for simulations using overset grid, and 0.96 m for deforming mesh simulations.

necessary to keep the cell aspect ratios around 1.0 in the vicinity of the free surface in order to accurately simulate breaking waves. Identified by the distance from a specific cell center to the moving boundary, the computational domain is divided into three regions: the inner region, middle region and outer region. The mesh cells in the inner region, which are close to the moving boundary, follow the motion of the rigid body. The mesh cells in the outer region are held stationary. The cells between the inner region and the outer region are moved based on the spherical linear interpolation (SLERP) of the body displacement. The SLERP method applied a cosine-like scale factor, a function of cell distance to the moving body boundary, to guarantee a smooth transition of cell movements between the inner and outer regions (Chen and Christensen, 2018).

The second method uses the overset mesh library in OpenFOAM (v2012), which is particularly suitable for applications involving large-amplitude motions (Chen et al., 2019; Windt et al., 2020). In the overset mesh method, two sets of grids are defined: one for a background mesh and one for a body-fitted overset mesh. A composite computational domain is then generated via cell-to-cell mappings between the two disconnected grids, which may arbitrarily overlap each other. The background mesh is stationary, while the overset mesh can move following the body motion, prescribed in advance or calculated according to Newton's second law. The cells in the entire domain are classified into three categories: *calculated*, *interpolated*, and *holes*. The flow governing equations are solved for *calculated* cells. The *interpolated* cells are employed to interpolate flow variables between the two mesh regions. The *holes* cells, which represent the moving body, are blocked out during the calculation. Because of the interpolation between different mesh regions, the overset mesh method may be more computationally demanding than the mesh deformation method (Windt et al., 2020).

2.4. Mooring dynamics model

In the lumped-mass formulation, the mass of the mooring line is discretized into point masses at nodes, assigning each node half the summed mass of the two adjacent line segments. The mooring line model MoorDyn combines internal axial stiffness and damping forces with weight and buoyancy forces, hydrodynamic forces from Morison's equation, and forces from contact with the seabed.

As described by Hall and Goupee (2015), each mooring line is

discretized into N equal-length segments consisting of $N+1$ nodes. The node index starts with 0 at the anchor and ends with $N+1$ at the fairlead. Each node is represented by a global position vector $\mathbf{r} = \mathbf{r}(x, y, z)$. Connecting two adjacent nodes \mathbf{r}_i and \mathbf{r}_{i+1} is segment $i+1/2$, the tangent of which is $\hat{\mathbf{q}}_{i+1/2}$ pointing from node i to node $i+1$,

$$\hat{\mathbf{q}}_{i+1/2} = \frac{\mathbf{r}_{i+1} - \mathbf{r}_i}{|\mathbf{r}_{i+1} - \mathbf{r}_i|} \quad (9)$$

The tension in the segment due to axial stiffness is

$$T_{i+1/2} = E \frac{\pi}{4} d^2 \epsilon_{i+1/2} \hat{\mathbf{q}}_{i+1/2} \quad (10)$$

where E is the Young's (elastic) modulus, d is the mooring line diameter, and $\epsilon_{i+1/2} = |\mathbf{r}_{i+1} - \mathbf{r}_i|/l - 1$ is the strain with l being the unstretched segment length.

The internal damping force in the segment which contributes to numerical stability is

$$C_{int} \frac{\pi}{4} d^2 \dot{\epsilon}_{i+1/2} \hat{\mathbf{q}}_{i+1/2} \quad (11)$$

where C_{int} is the internal damping coefficient, and $\dot{\epsilon}_{i+1/2} = \partial \epsilon_{i+1/2} / \partial t$ is the strain rate.

The hydrodynamic forces including drag and added mass are calculated using the Morison equation, applied directly at node i . The tangent at node i , $\hat{\mathbf{q}}_i$, is approximated as a unit vector along a line passing through its two adjacent nodes

$$\hat{\mathbf{q}}_i = \frac{\mathbf{r}_{i+1} - \mathbf{r}_{i-1}}{|\mathbf{r}_{i+1} - \mathbf{r}_{i-1}|} \quad (12)$$

The drag force acting on node i is composed of a transverse component, \mathbf{D}_{ni} , and a tangential component, \mathbf{D}_{ti} ,

$$\mathbf{D}_{ni} = 0.5 \rho C_{dn} dl |(\dot{\mathbf{r}}_i \cdot \hat{\mathbf{q}}_i) \hat{\mathbf{q}}_i - \dot{\mathbf{r}}_i| ((\dot{\mathbf{r}}_i \cdot \hat{\mathbf{q}}_i) \hat{\mathbf{q}}_i - \dot{\mathbf{r}}_i) \quad (13)$$

$$\mathbf{D}_{ti} = 0.5 \rho C_{dt} dl |(-\dot{\mathbf{r}}_i \cdot \hat{\mathbf{q}}_i) \hat{\mathbf{q}}_i| (-\dot{\mathbf{r}}_i \cdot \hat{\mathbf{q}}_i) \hat{\mathbf{q}}_i \quad (14)$$

where C_{dn} is the transverse drag coefficient, C_{dt} is the tangential drag coefficient, and $\dot{\mathbf{r}}_i$ is the mooring line node velocity. Note that these forces are calculated assuming quiescent water; wave kinematics are excluded by MoorDyn at the moment. Hence the relative velocity (acceleration) between fluid and mooring node is $-\dot{\mathbf{r}}_i$ ($-\ddot{\mathbf{r}}_i$) in this case.

Similarly, the added mass force is composed of a transverse

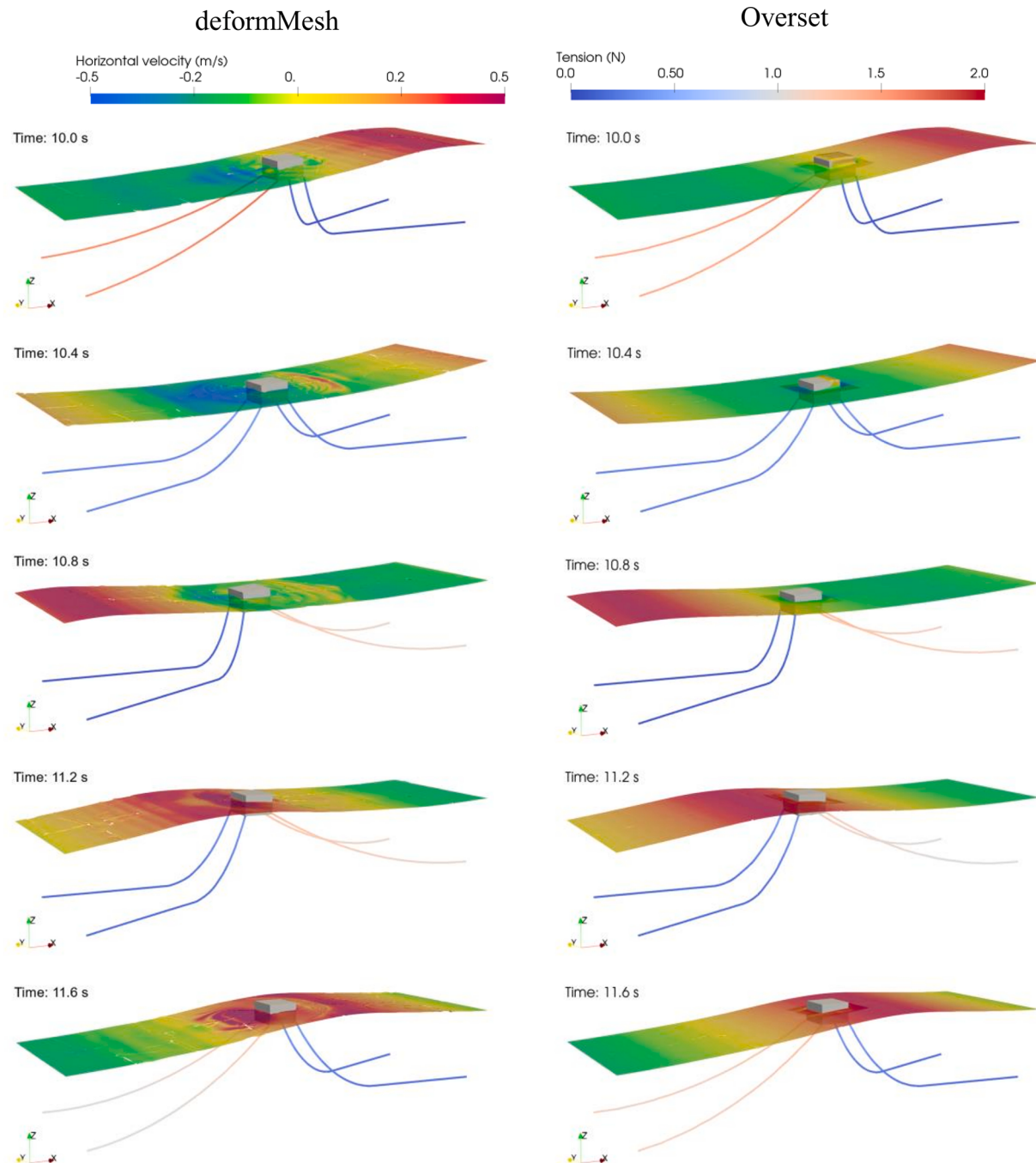


Fig. 4. Instantaneous free surface (iso-surface $\alpha = 0.5$; color: horizontal flow velocity) and a four-point catenary mooring system configuration (color: mooring line tension) over one wave cycle for a floating box interacting with regular waves for case H12T20. Left column: mesh deformation simulation; right column: overset simulation.

component and a tangential component, which can then be combined into a 3×3 added mass matrix for node i ,

$$\mathbf{a}_i = \mathbf{a}_{ni} + \mathbf{a}_{ti} = \rho \frac{\pi}{4} d^2 l [C_{an} (\mathbf{I} - \hat{\mathbf{q}}_i \hat{\mathbf{q}}_i^T) + C_{at} (\hat{\mathbf{q}}_i \hat{\mathbf{q}}_i^T)] \quad (15)$$

where C_{an} and C_{at} are the transverse and tangential added mass coefficients, respectively.

The mooring line seabed interaction is modeled by a linear spring-damper approach. When a node touches the seabed (i.e. $z_i \leq z_b$), a vertical reaction force is applied to that node

$$\mathbf{B}_i = ld[(z_b - z_i)k_b - \dot{z}_i c_b] \hat{\mathbf{e}}_z \quad (16)$$

where k_b and c_b are the seabed stiffness and damping coefficient, z_b is the seabed elevation, z_i and \dot{z}_i are the node vertical coordinate and velocity, and $\hat{\mathbf{e}}_z$ is a unit vector in the positive z direction.

Combining the above forces with submerged weight, \mathbf{W}_i , the complete equation of motion for each node i (with a lumped mass, m_i) is

$$(m_i \mathbf{I} + \mathbf{a}_i) \ddot{\mathbf{r}}_i = \mathbf{T}_{i+1/2} - \mathbf{T}_{i-1/2} + \mathbf{C}_{i+1/2} - \mathbf{C}_{i-1/2} + \mathbf{W}_i + \mathbf{B}_i + \mathbf{D}_{ni} + \mathbf{D}_{ti} \quad (17)$$

This system of equations for all nodes of the mooring lines is solved using a constant-time-step second-order Runge–Kutta integration algorithm.

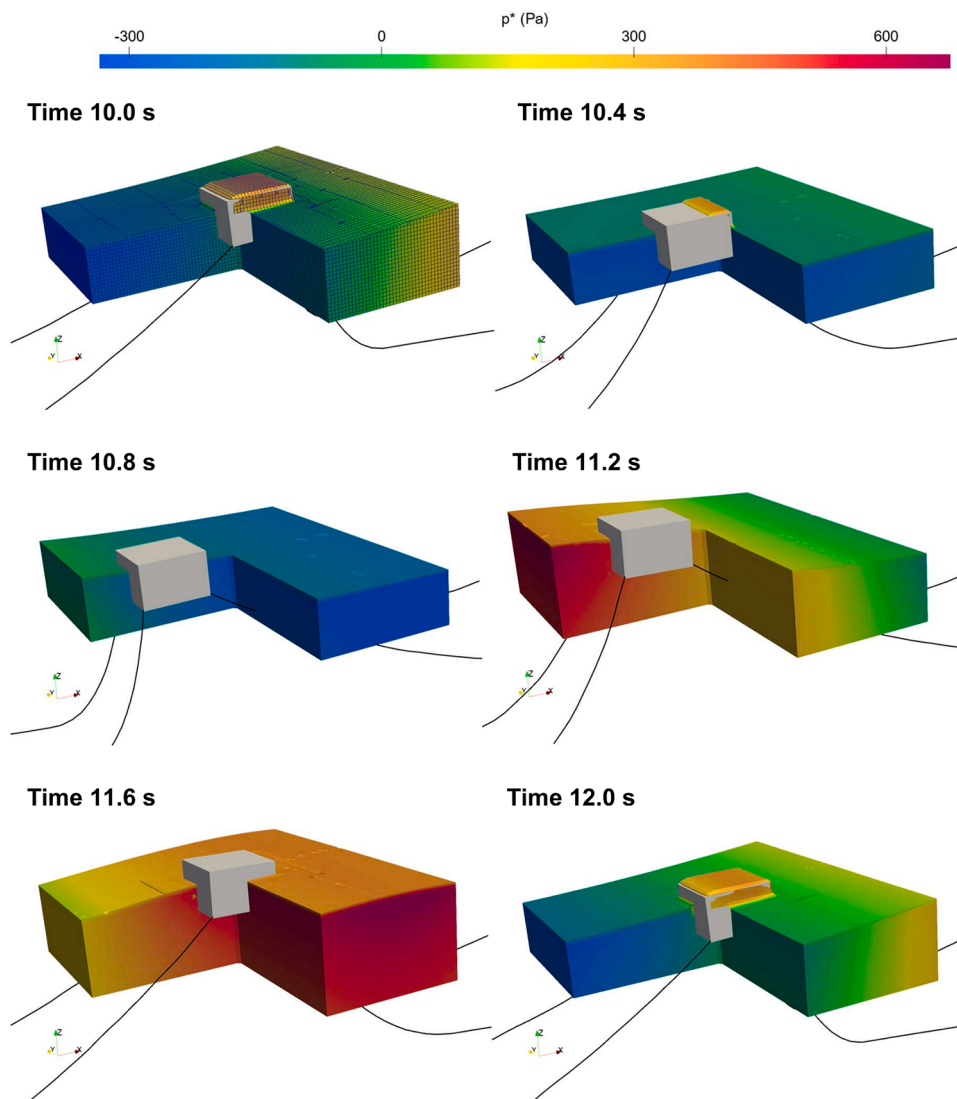


Fig. 5. Close-up view of instantaneous dynamic pressure (p^*) field in the vicinity of the floating box and the catenary mooring system configuration over one wave cycle for case H12T20 using overset simulation. The computational mesh is demonstrated for time instant 10.0 s only; some blurred regions exist where the overset grid and the background mesh overlap.

2.5. Coupling MoorDyn with floating body motion

The coupling of floating body motion with free surface flow is achieved in a segregated manner with a PIMPLE loop, which is a combination of SIMPLE and PISO algorithms. The PIMPLE loop within each time step helps to alleviate the time lag between the flow and the body motion. For each PIMPLE iteration, the floating body motion is solved first and the moving mesh updated. The VOF function is then advected to capture the air-water interface. The pressure-velocity coupling is resolved with a PISO loop, which consists of one optional momentum predictor and several pressure corrections. The coupling of MoorDyn with floating body motion solver follows a loose-coupling approach. A six DoFs rigid body restraint called *moorDynR* is implemented in the body motion solver, which calls MoorDyn to initialize the mooring system the first time the mooring forces are requested. The position and velocity of the floating body are passed from the body motion solver to MoorDyn, which then calculates the fairlead kinematics and updates the mooring system states such as mooring line nodes' position/velocity and segments tension. The mooring restraining forces and moments acting on the floating body, calculated by summing contributions from all fairlead tensions, are returned from MoorDyn to *moorDynR* and then to the body motion solver to update the body acceleration. A couple of

PIMPLE iterations may be needed to help converge the floating body motion and the mooring system states. The new rigid body restraint was compiled into a dynamic library that can be simply loaded into the existing flow solvers *interDyMFoam* and *overInterDyMFoam* at run time.

It should be noted that this partitioned CFD/6-DoF solver, where the floating body motion is obtained by solving the Navier-Stokes and 6-DoF motion equations separately, is known to be subject to instabilities due to artificial added mass which is predominately affected by the fluid-body density ratio and the time step size (Förster et al., 2007). The solution to this issue is to implement a tighter coupled solver (e.g. Gatin et al., 2017), allowing the fluid and the body motion to be more converged before the simulation advances to the next time step. Applying a dynamic relaxation to the body acceleration, fluid pressure, or integrated body force/moment is found to increase the numerical stability (Bruinsma et al., 2018; Tsai et al., 2021).

2.6. Two alternative mooring models: MAP++ and Moody

Besides the lumped-mass model MoorDyn, the present paper also coupled a quasi-static mooring model MAP++ (Masciola et al., 2013) and a higher-order finite element model Moody (Palm et al., 2017) with the floating body motion solver *sixDoFRigidBodyMotionSolver* in

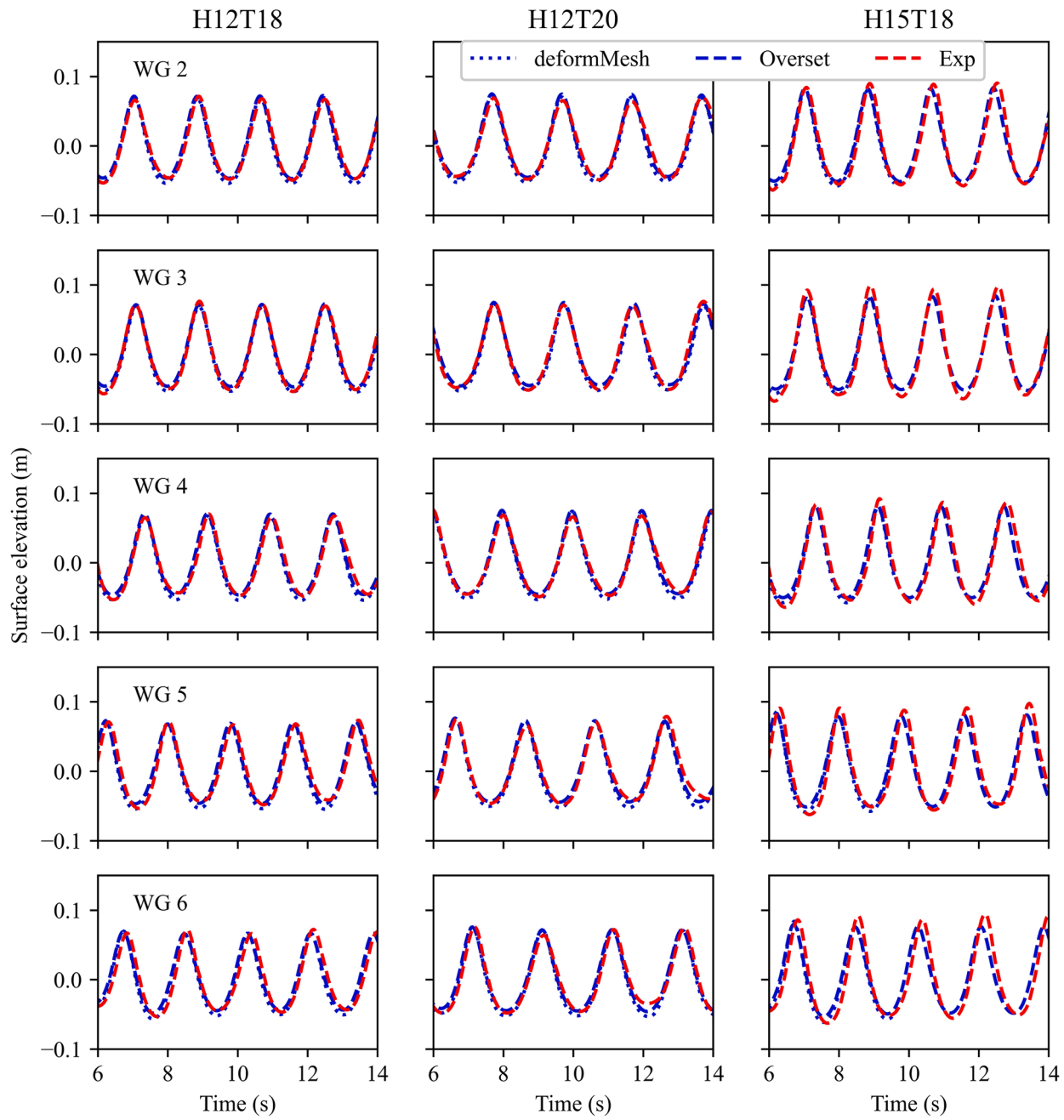


Fig. 6. Surface elevation by the deforming mesh method (dotted lines) and overset grid method (dashed lines).

OpenFOAM. Table 1 lists the main features of the three mooring codes. The Mooring Analysis Program (MAP++) is an open-source project developed by the National Renewable Energy Laboratory (NREL). The multisegmented, quasi-static mooring model was developed based on an extension of conventional single line catenary solutions, allowing multielement mooring systems with arbitrary connection configurations to be analyzed. Forces arising from inertia, viscous drag, internal damping, and bending are neglected. Static equilibrium is achieved when the connection point forces from individual catenary mooring lines sum to zero. Moody is a finite element mooring dynamics model developed with the special intent of capturing and resolving snap loads. It uses an *hp*-adaptive discontinuous Galerkin method; the high-order formulation makes engineering accuracy achievable using only a few high order elements. External forces acting on the cables include the added mass and Froude-Krylov forces, the drag force, the net force of gravity and buoyancy, and seabed contact forces. Cable bending stiffness

is neglected, however. Moody's code itself is not open source, but a precompiled shared library has been provided that can be linked with third-party software. Readers are referred to the original references for detailed descriptions of the two mooring models (Masciola et al., 2013; Palm et al., 2017).

Instead of the floating body's position/velocity as in the MoorDyn coupling, the mooring fairlead positions (calculated from the instantaneous orientation of the floating body) were passed to the two mooring models to update the mooring system states. Correspondingly, instead of the total mooring forces/moments exerting on the floating body, the fairlead tensions from all the mooring lines were returned from the two mooring models to the rigid body restraint *sixDoFRigidBodyMotionRestraint*. The restraint then calculated the total mooring forces/moments and passed them to the motion solver to update the body motion. The comparison between these models will be presented in the results section.

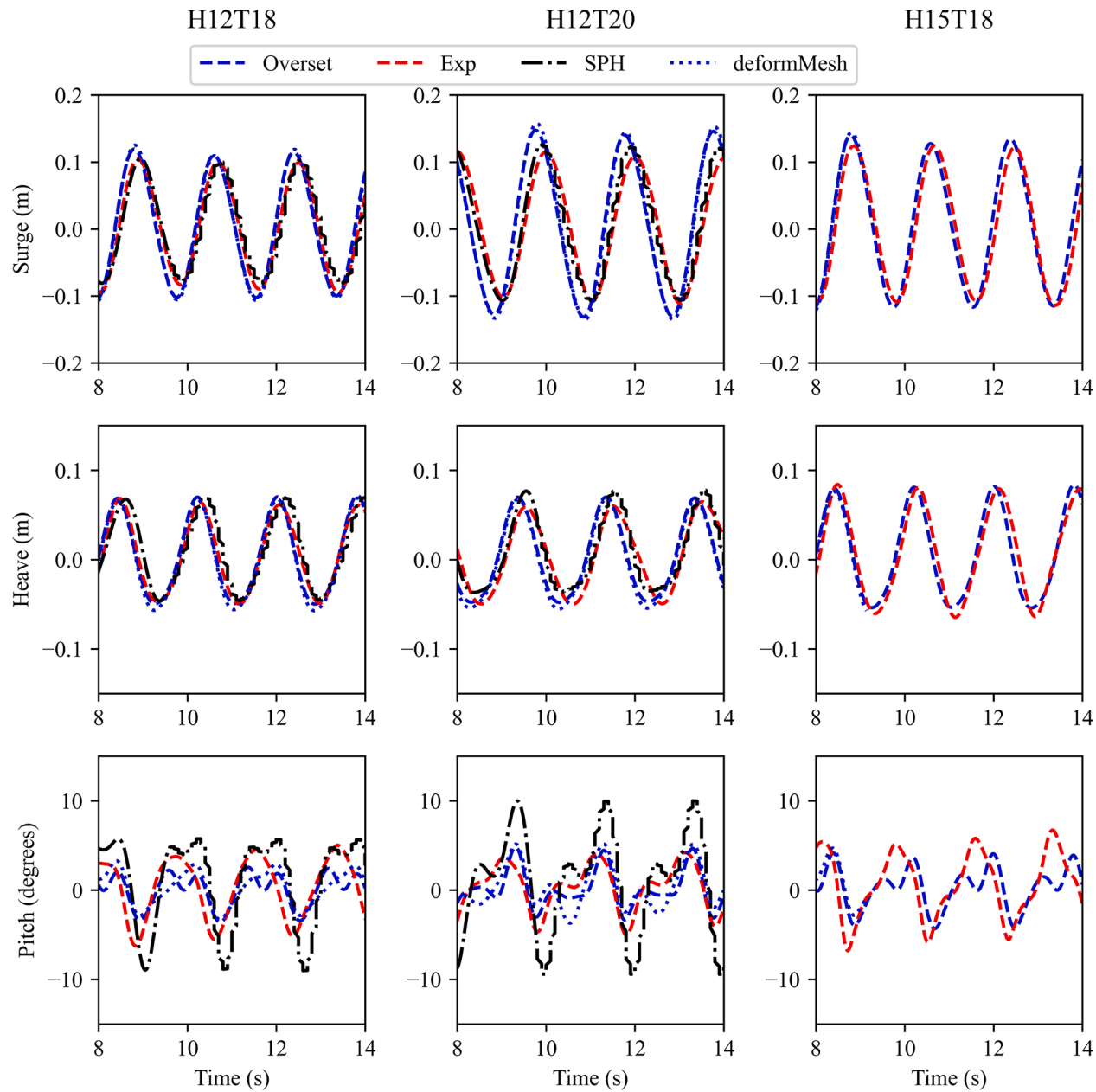


Fig. 7. Floating box motion (first row: surge; second row: heave; third row: pitch) for the three regular wave cases: H12T18, H12T20, H15T20. Blue dashed lines: overset grid simulations; blue dotted lines: deforming mesh simulations; dash-dotted lines: SPH results by Dominguez et al. (2019).

3. Results

3.1. Experimental data

Experimental results used in this study are from tests in a 30.0 m long, 1.0 m wide and 1.2 m high wave flume (Wu et al., 2019), which was equipped with second-order wave generation and absorption techniques. This experimental campaign, which was part of the European MaRINET2 Esflowc project, studied the motions and mooring line responses of a floating oscillating water column WEC and a simple solid box subjected to regular waves. The dataset generated served as a good source of validation for numerical model development. The experimental data include motions of the moored floating body (heave, surge, and pitch), mooring anchor tensions for the front and rear mooring lines, and free-surface elevations at different locations within the wave flume. The measurements for the solid box are used to validate the coupled model described in Section 2.

The solid box is 20 cm long, 20 cm wide, and 13.2 cm high. The box is made of light PVC material and has a combined mass of 3.16 kg with connections included (see Table 2 for a list of the box's and the mooring lines' properties). A wood plate was attached to the front face of the box, on which reflective markers were installed to enable a 6-DOF motion optical tracking system. The box is symmetric in three principal axes; its center of gravity is thus the geometrical center of the box and the cross components of the inertia matrix are zero. When freely floating the box had a draft of 0.0786 m; about 60% of the box height was submerged. A four-point symmetric slack mooring system connected the floating box to the wave flume bottom. The anchor of each mooring line was connected to a load cell on the flume bottom with the axis of measurement oriented horizontally to measure only the horizontal component of the mooring line tension at its anchoring point (Dominguez et al., 2019). On the fairlead side, each mooring line was connected to an iron hook 0.5 cm above the box bottom. Table 3 lists the coordinates of the anchoring location and fairlead connections of the four mooring lines (iron chains).

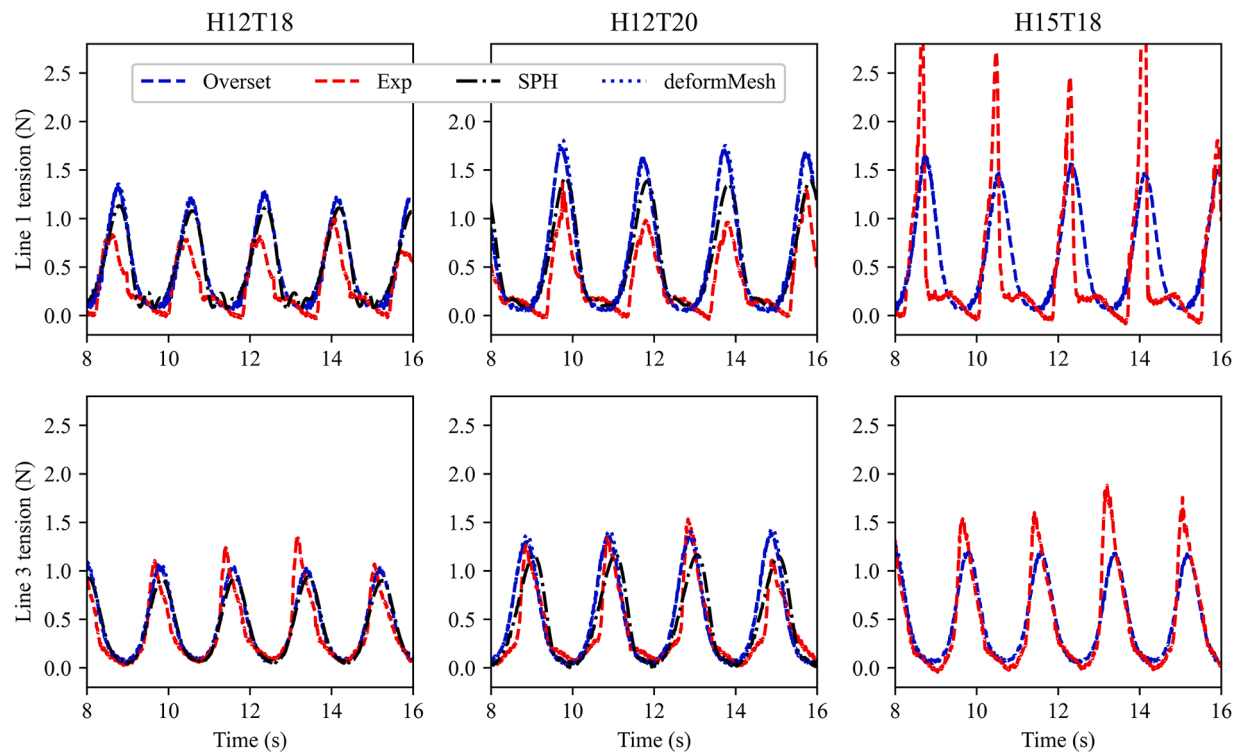


Fig. 8. Comparison of mooring anchor tensions in the front line (Line 1, first row) and rear line (Line 3, second row) for the three regular wave test cases. Blue dashed lines: overset grid simulations; blue dotted lines: deforming mesh simulations; dash-dotted lines: SPH results by Dominguez et al. (2019).

Table 4 shows the incident regular wave conditions of the tests used to validate the coupled model. There were no free decay data for this set of experiments. From our numerical (2D) simulation results, the box's heave period is about 0.82 s (the mooring system has negligible effect); the pitch period is about 1.26 s without moorings and 1.0 s with moorings. Note that previous studies have shown that the pitch response is very sensitive to the box's center of gravity and moment of inertia (Palm et al., 2016; Martin et al., 2020). The wave conditions considered in this study are outside the resonance region. The water surface elevations were registered using resistive wave gauges (WGs). The specific locations of the WGs within the numerical flume (see Fig. 3b) are listed in Table 5.

3.2. Numerical model setup

Fig. 3 shows the numerical model setup that matches the experiment. A global coordinate system is defined with the positive x -axis following the wave propagation direction (from left to right) and the positive z -axis pointing upwards. Horizontally $x = 0$ and $y = 0$ is located at the box's geometric center, and vertically $z = 0$ is defined at the still water level. Note that this global coordinate system is reversed in comparison with the experiments (see Fig. 2 in Wu et al., 2019), in which the waves propagated from right to left. Instead of simulating the wave absorption beach in the physical wave flume, a cell stretching area is defined for the rightmost 3 m of the numerical flume, which reduces the overall grid number and helps damp the waves.

The computational domain is 10 m long, 1 m wide, and 0.957 m high for the deforming mesh grid. A grid convergence study was conducted to determine the proper mesh size while avoiding unreasonably long simulation times (see the Appendix for results). A uniform grid size of 0.01 m \times 0.01 m \times 0.011 m is applied across $x = [-3.5, 3.5]$ m, $y = [-0.25, 0.25]$ m, and $z = [-0.28, 0.8]$ m. A graded mesh is applied across the remaining domain. The range of grid size is 0.01–0.2 m in the x direction, 0.01–0.031 m in the y direction, and 0.01–0.03 m in the z direction. The computational domain for the overset grid is 0.8 m high. Similarly, a

uniform grid size of 0.01 m \times 0.01 m \times 0.01 m is applied across the center of the domain for the background mesh. The overset mesh enclosing the floating box spans $x = [-0.2, 0.2]$ m, $y = [-0.2, 0.2]$ m, and $z = [-0.18, 0.15]$ m, which is discretized uniformly by $40 \times 40 \times 30$ grids. The overall grid number is about 5 million for the deforming mesh, and 4.6 million for the overset mesh.

The active generating-absorbing wavemaker *IHFoam* is applied to the inlet and outlet boundaries of the numerical wave flume (Higuera et al., 2013). The 3D computational domain is decomposed into 32 sub-domains for overset simulations and up to 72 sub-domains for deforming mesh simulations. It was run on the UNM Gibbs cluster with the Scientific Linux operating system and Intel Xeon processors (E5-2670@2.6 GHz). The simulation was intended to run for 16 s (up to 8 wave periods) and the time step was adjusted at runtime with a maximum Courant number limit of 0.5. The Euler scheme was used for time marching. Other discretization schemes followed the standard practices of wave simulations using OpenFOAM's *interFoam* series of solvers. For each time step, 3 outer correctors (PIMPLE iterations) were used along with two pressure correctors (no momentum predictor) per PISO loop. To avoid numerical instabilities, the floating body acceleration was relaxed by a factor of 0.8 and no acceleration damping was applied. This under-relaxation of body acceleration is a compromise between accuracy and stability. For deforming mesh simulations, cell deformations are allowed only within a region defined by an inner distance of 0.05 m and an outer distance of 0.35 m (relative to the moving body). A non-orthogonal corrector of 1 was used to account for the mesh non-orthogonality as a result of the mesh deformation. No turbulence models were switched on for the simulation results presented in this paper, which eased the mesh generation and reduced the computational overhead in the absence of very fine grids required in the body boundary layers. However, the overset grid results for case H15T18 (the steepest wave) with the $k - \omega$ SST turbulence model switched on are virtually the same. The inclusion of detailed turbulence modelling and resolving of the body boundary layers will be investigated in future work.

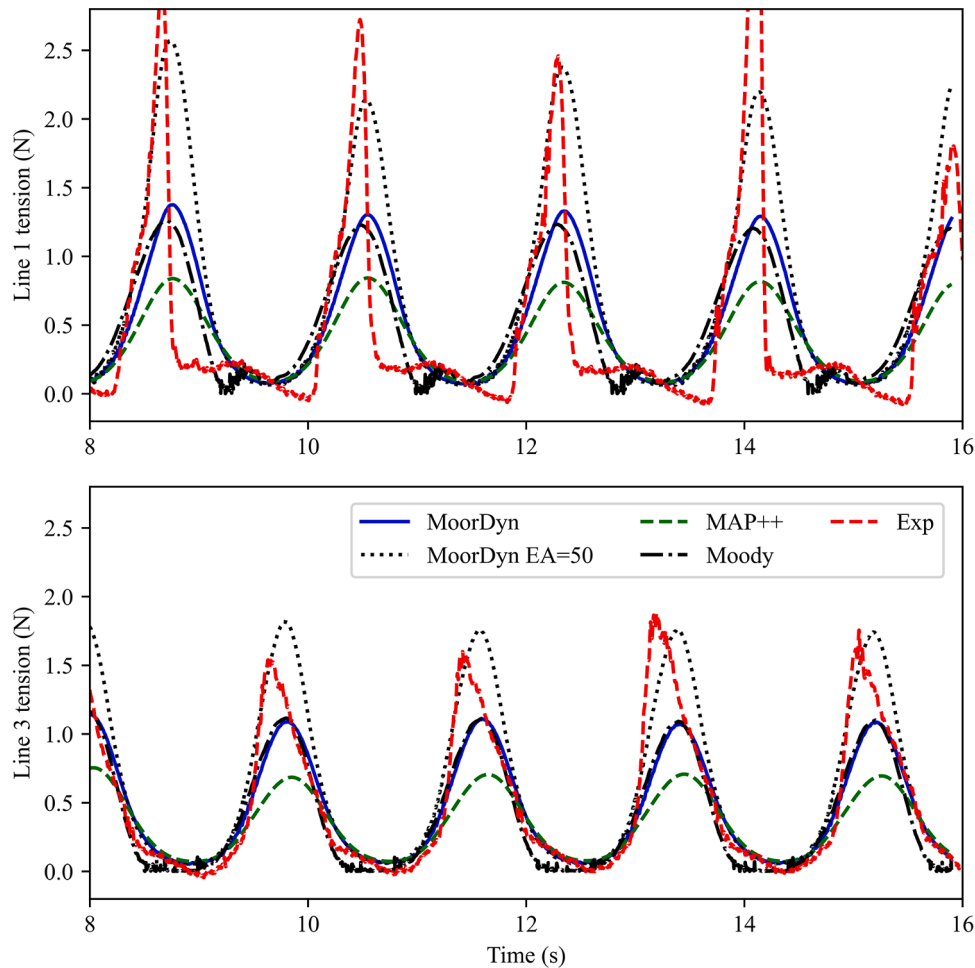


Fig. 9. Comparison of mooring line anchor tension between different models: lumped-mass model MoorDyn, quasi-static model MAP++, and finite element model Moody. All models used an axial stiffness of $EA = 29$ N for the mooring lines, except for the dotted lines where axial stiffness increased to $EA = 50$ N in the MoorDyn simulation.

The modeling settings for the mooring lines follow those used by Dominguez et al. (2019), which coupled an older version of MoorDyn with DualSPHysics. Specifically, each mooring line was discretized with 40 segments. To match the experimental tension response of the lines, Dominguez et al. (2019) adjusted the line's modulus of elasticity to $E = 2.78$ MPa, resulting in an axial stiffness of $EA = 29$ N (product of elastic modulus E and cross-sectional area A). The line internal damping coefficient was set to give a damping ratio of 80% for each segment. The added mass coefficient was 1.0 in the transverse direction and zero in the axial direction. The drag coefficient was 1.6 in the transverse direction and 0.05 in the axial direction. The initial pretension at the mooring anchor points calculated by MoorDyn was 0.31–0.32 N, in agreement with the experimental measurements.

The computational time for the overset simulations (32 CPUs) is about 32, 36, and 29 hrs for the 3 cases. The computational time for the deforming mesh simulations is significantly longer, more than twice the time needed for overset simulations. The simulations of case H12T18 and H12T20 were terminated at physical time 10.5 s and 15.6 s, respectively, after running 72 hrs with 32 CPUs. A rerun of case H12T18 was terminated at physical time 14.5 s after running 58 hrs with 72 CPUs. And a rerun of case H12T20 was completed after running 60 hrs with 64 CPUs. The simulation of case H15T18 was never completed, which was terminated around 9.2 s.

Fig. 4 shows the snapshots over one wave period of the instantaneous free surface and the mooring lines for case H12T20. The color of the free surface (iso-surface $\alpha = 0.5$) corresponds to the value of the horizontal flow velocity at the free surface. The color of the mooring lines denotes

the instantaneous tension within each segment along the mooring lines. It is noticeable that the flow field predicted by the mesh deformation simulation, likely due to the resulting mesh non-orthogonality, is more disturbed in the vicinity of the floating box than that by the overset simulation. Fig. 5 shows a close-up view of instantaneous dynamic pressure, p^* in Eq. (2), in the vicinity of the floating box over one wave cycle for the same case using overset simulation. Wave overtopping is observed briefly as slight amount of water runs up from the lateral sides (normal to the y-axis) of the box (see also supporting video animation). Fig. 6 shows the comparison of the surface elevation history registered by the wave gauges numerically and experimentally for all the three cases. There are overall good agreements for both the deforming mesh and the overset grid simulations.

3.3. Floating box motion

Fig. 7 shows the comparison of the floating box motion (surge, heave, and pitch) for the three test cases H12T18, H12T20, and H15T20. Satisfactory agreements were obtained in heave motion predictions, while some discrepancies were present in surge and pitch motions. Considering the good comparisons by 2D simulations in the appendix, the boundary layer modeling on the lateral sides (normal to the y-axis) of the box and the 3D numerical wave tank setup may contribute to some of the discrepancies here. For the same wave period of $T = 1.8$ s (cases H12T18 and H15T18), a larger wave of $H = 0.15$ m results in better surge predictions than the smaller wave of $H = 0.12$ m, which slightly over-predicts the surge motion. Despite the different meshing

techniques used to accommodate the floating body motion, both the deforming mesh and the overset mesh simulations were able to predict consistent surge and heave motions but slightly different pitch motions. It is understood that the body-conforming mesh required in the deforming mesh simulations is responsible for this small discrepancy in pitch motion. The pitch motion was slightly underpredicted by the present OpenFOAM model and it was overpredicted by DualSPHysics (Domínguez et al., 2019). The measuring uncertainties in box mass, and especially in center of gravity and moment of inertia of the floating box may contribute to some of the differences (Palm et al., 2016; Martin et al., 2020). More importantly though, a high wood plate supporting camera markers was attached to the front face of the box in the experiments. The absence of this plate in the numerical model may account for some of the discrepancies as well. It was observed during the physical tests that water splashed onto this plate (Domínguez et al., 2019).

3.4. Mooring line tension

As described in Sections 2.4~2.6, a total of three mooring codes (MoorDyn, MAP++, and Moody) are coupled with the floating body 6-DoF motion solver in OpenFOAM. MoorDyn is a lumped-mass model (Hall and Goupee, 2015), MAP++ is a quasi-static mooring model (Masciola et al., 2013), and Moody is a higher-order finite element model. In this section, we will first present the mooring line tension response predicted by MoorDyn for the three regular wave cases listed in Table 4. Then the performance of the three mooring solvers are compared and discussed for only one case (H15T18) with the most nonlinear and steepest waves. Fig. 8 shows the mooring anchor tensions for one front line and one rear line (Line 1 and Line 3 in Fig. 3d); the tensions in the other lines are similar since this is a 4-point symmetric mooring system. The predictions by the present model and DualSPHysics are comparable since both models used MoorDyn as the mooring system solver. The slightly larger tension by the present model, for the front lines in particular, is caused by the over-prediction of the box's surge motion (Fig. 7).

The anchor tensions measured in the rear lines are in general smoother than those in the front lines. The tensions in the front lines are more dynamic, with snap load conditions occurring particularly for cases H12T20 and H15T18. For cases H12T18 and H12T20, the anchor tension measured in the front lines were counter-intuitively smaller than those in the rear lines. Both the present OpenFOAM model and the DualSPHysics model coupling with MoorDyn predicted the rear line tensions reasonably well, but they somewhat failed to capture the highly dynamic behavior of the anchor tension in the front lines. For case H15T18, the anchor tension in the front lines was severely underpredicted. All these indicate that there is some experimental setup that is missed or mis-represented in the numerical models. More discussions will follow at the end of this section. Though the mooring line tension was under-predicted, the floating box's motion (see the last column in Fig. 7) compares remarkably well with the experimental data. This demonstrates on the other hand that the mooring tension response has relatively small effects on the floating box's motion response.

Fig. 9 shows the comparison of anchor tensions for case H15T18 between different mooring models: MoorDyn, MAP++, and Moody. All the three models used the same mooring line settings as described in Section 3.2. It is seen that the quasi-static model MAP++ underpredicted the tension in both the front and the rear lines, which is expected since the mooring dynamics effects are ignored in this model. Both MoorDyn and Moody gave consistent tension predictions when the same input was used for the mooring system. The finite element model Moody, however, made no better tension predictions than the lumped-mass model MoorDyn, although Moody was developed with the special intent of resolving snap loads in mooring cables (Palm et al., 2017). This indicates that apart from snap loads modeling, there are other factors that are contributing to these discrepancies. The largest source of error comes from the various approximations made to numerically

model the mooring lines (made of iron chains in this case), such as mooring line axial stiffness, empirical hydrodynamic (added mass and drag) coefficients, and seabed friction. Also shown in Fig. 9 is the MoorDyn result with the axial stiffness (EA) being increased from 29 N to 50 N, which adequately captured the tension magnitudes in both the front and rear lines. It should be noted that using $EA = 50$ N for the other two cases will result in much larger tensions than those measured by the experiments. After all, $EA = 29$ N is what Domínguez et al. (2019) had derived in order to match the experimental tension response of the mooring lines.

The mooring line elasticity of 2.78 MPa used in the present study, as manually tuned by Domínguez et al. (2019), is much less than that for a typical metal material. It may be affected by chain links deformation (not welded shut at this small scale) and by additional elasticity caused by chain end connections and load cell deformation. The mooring line chain ring was connected to the load cell with two tight cable ties on the flume bottom and to the floating box through an eye hook. As Domínguez et al. (2019) pointed out, both MoorDyn and Moody are not able to represent a mooring line being attached to or running through an iron hook, nor the elasticity and loose behavior of cable ties used to make end connections. All these detailed mooring system setups may be responsible for the numerical models' failure to reproduce the sudden increase of tensions in the front lines (Fig. 8). In all the simulations presented, the hydrodynamic forces (inertia and drag forces) acting on the mooring line segments were calculated assuming quiescent water. Thus, the mooring line tension may be under-estimated when the floating body is subjected to steep waves. Extracting flow motion from the CFD model and feeding them into the mooring model is an ongoing work.

4. Conclusions

This paper incorporated a lumped-mass based mooring dynamics model, MoorDyn, into the floating body motion solver in the CFD toolbox, OpenFOAM. The coupling of the two open-source libraries complements the current practices of representing the mooring system merely by a quasi-static mooring model. Because of the modular structure of the OpenFOAM library, both mesh deformation and overset grid method can be used as the mesh motion solver in the CFD model to account for the floating body motion. The coupled model was validated against experimental measurements for a floating box moored with four catenary lines in regular waves. Comparable results were achieved by the two mesh motion methods. In addition to the lumped-mass mooring model, the present work also coupled a quasi-static mooring model MAP++ and a higher-order finite element model Moody with the floating body motion solver in OpenFOAM. The mooring line tensions predicted by MoorDyn and Moody were consistent, while the tensions by MAP++ tend to be under-predicted. Some discrepancies were observed though due to the necessary approximations made to numerically model the chain mooring lines at such a small scale. For example, details of chain attachments and anchor/fairlead connections in the experimental setup cannot be reproduced in the numerical model. For all the simulations in this work, the hydrodynamic forces on mooring lines neglected the effect of wave kinematics; the forces were caused by the mooring line motion in quiescent water. Extracting flow motion from the CFD solver and feeding them into the mooring dynamics model is an ongoing work, which entails customizing and recompiling the flow solver. The coupling code developed in this work is open-source and publicly available. The coupled CFD/6-DoF motion solver model equipped with three mooring line codes (MoorDyn, MAP++, and Moody) may be used to carry out survivability studies of FOWTs and WECs subject to severe sea states. It is expected that CFD simulations using overset grids are particularly capable of handling the large amplitude motions of moored floating bodies in highly nonlinear breaking waves.

CRediT authorship contribution statement

Haifei Chen: Conceptualization, Methodology, Software, Validation, Data curation, Visualization, Writing – original draft, Writing – review & editing. **Matthew Hall:** Software, Writing – review & editing.

Declaration of Competing Interest

The authors declare that they have no known competing financial interests or personal relationships that could have appeared to influence the work reported in this paper.

Acknowledgement

The authors would like to thank the UNM Center for Advanced Research Computing, supported in part by the National Science Foundation, for providing the research computing resources used in this work. The authors would also like to thank Drs. Minghao Wu and

Alejandro Crespo for providing the experimental and DualSPHysics simulation data. The coupling code developed in this work can be accessed at <https://gitlab.com/hfchen20/foamMooring>.

Supplementary materials

Supplementary material associated with this article can be found, in the online version, at doi:[10.1016/j.apor.2022.103210](https://doi.org/10.1016/j.apor.2022.103210).

Appendix. Grid convergence study

To save computational time, 2D simulations were conducted for grid convergence study. Three grid resolutions were selected for both the deforming mesh and the overset grid simulations. For the deforming mesh simulations, the medium grid size was uniformly 0.01 m x 0.011 m across the computational domain, except for the rightmost 3 m where cell stretching with a ratio of 1.07 was applied to reduce the grid numbers and damp the waves. For overset grid simulations, the medium

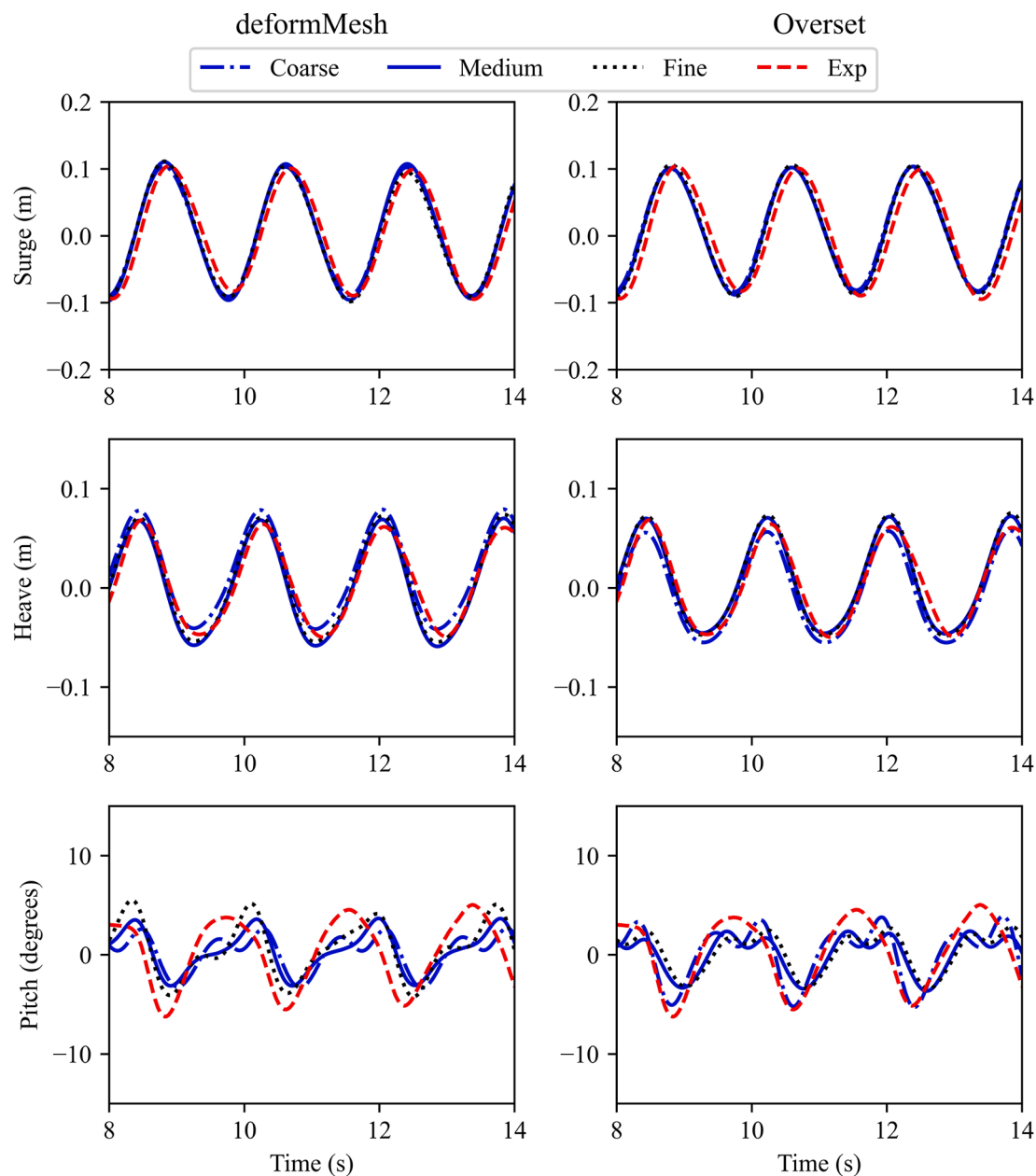


Fig. A1. Comparison of floating box motions by three grid resolutions for case H12T18.

grid size was uniformly 0.01 m x 0.01 m for both the background mesh and the overset mesh. The size of the coarse/fine grid was twice/half that of the medium grid.

Fig. A1 shows comparison of the box motion by the two mesh motion methods for case H12T18. The surge motions, for which the mooring system provides the only restoring force, were indistinguishable between the three grid results. The heave motions converged between the medium and fine grid size. For the pitch motions, the results by deforming mesh method, were more sensitive to grid resolutions than the overset grid method. This sensitivity is likely related to the body-conforming grid of the deforming mesh method, for which finer grids may be required to adequately resolve the boundary layers near the body surface. But overall, the medium grid size was able to capture the box motion well and so was selected in the ensuing 3D simulations. The 2D results from this grid convergence study show that the 3D effects are actually not significant for cases considered in this paper, since the box dimensions (0.2 m) are small relative to the incoming wave length (>3.57 m). The floating box has the same dimensions in x - and y -directions, so the results from the 2D grid convergence analysis justify the grid sizes selected for the 3D simulations.

References

- Bruinsma, N., Paulsen, B.T., Jacobsen, N.G., 2018. Validation and application of a fully nonlinear numerical wave tank for simulating floating offshore wind turbines. *Ocean Eng.* 147, 647–658.
- Dalrymple, R.A., Rogers, B.D., 2006. Numerical modeling of water waves with the SPH method. *Coastal Eng.* 53 (2–3), 141–147.
- Chen, L., Basu, B., Nielsen, S.R.K., 2018. A coupled finite difference mooring dynamics model for floating offshore wind turbine analysis. *Ocean Eng.* 162, 304–315.
- Chen, H., Christensen, E.D., 2018. Simulating the hydrodynamic response of a floater-net system in current and waves. *J. Fluids Struct.* 79, 50–75.
- Chen, H., Qian, L., Ma, Z., Bai, W., Li, Y., Causon, D., Mingham, C., 2019. Application of an overset mesh based numerical wave tank for modelling realistic free-surface hydrodynamic problems. *Ocean Eng.* 176, 97–117.
- Cheng, P., Huang, Y., Wan, D., 2019. A numerical model for fully coupled aero-hydrodynamic analysis of floating offshore wind turbine. *Ocean Eng.* 173, 183–196.
- Domínguez, J.M., Crespo, A.J., Hall, M., Altomare, C., Wu, M., Stratigaki, V., Gómez-Gesteira, M., 2019. SPH simulation of floating structures with moorings. *Coastal Eng.* 153, 103560.
- Förster, C., Wall, W.A., Ramm, E., 2007. Artificial added mass instabilities in sequential staggered coupling of nonlinear structures and incompressible viscous flows. *Comput. Meth. Appl. Mech. Eng.* 196 (7), 1278–1293.
- Gatin, I., Vukčević, V., Jasak, H., Rusche, H., 2017. Enhanced coupling of solid body motion and fluid flow in finite volume framework. *Ocean Eng.* 143, 295–304.
- Hall, M., Buckingham, B., Crawford, C., 2014. Evaluating the importance of mooring line model fidelity in floating offshore wind turbine simulations. *Wind Energy* 17 (12), 1835–1853.
- Hall, M., Goupee, A., 2015. Validation of a lumped-mass mooring line model with DeepCwind semisubmersible model test data. *Ocean Eng.* 104, 590–603.
- Hall, M., 2020. MoorDyn V2: New Capabilities in Mooring System Components and Load Cases. In: ASME 2020 39th International Conference on Ocean, Offshore and Arctic Engineering. American Society of Mechanical Engineers Digital Collection.
- Hall, M., Sirinivas, S., Yu, Y.H., 2021. Implementation and Verification of Cable Bending Stiffness in MoorDyn. In: International Conference on Offshore Mechanics and Arctic Engineering (Vol. 84768, p. V001T01A011). American Society of Mechanical Engineers.
- Higuera, P., Lara, J.L., Losada, I.J., 2013. Realistic wave generation and active wave absorption for Navier–Stokes models: Application to OpenFOAM®. *Coastal Eng.* 71, 102–118.
- Hirt, C.W., Nichols, B.D., 1981. Volume of fluid (VOF) method for the dynamics of free boundaries. *J. Comput. Phys.* 39 (1), 201–225.
- Huang, H., Chen, H.C., 2021. Coupled CFD-FEM simulation for the wave-induced motion of a CALM buoy with waves modeled by a level-set approach. *Appl. Ocean Res.* 110, 102584.
- Jacobsen, N.G., Fuhrman, D.R., Fredsøe, J., 2012. A wave generation toolbox for the open-source CFD library: OpenFOAM®. *Int. J. Numer. Methods Fluids* 70 (9), 1073–1088.
- Jasak, H., 1996. Error analysis and estimation for the finite volume method with applications to fluid flows. Imperial College of Science, Technology and Medicine. Ph.D. thesis.
- Jasak, H., Tuković, Ž., 2010. Dynamic mesh handling in OpenFOAM applied to fluid-structure interaction simulations. In: *Proceedings of the V European Conference on Computational Fluid Dynamics ECCOMAS CFD 2010*.
- Johanning, L., Smith, G.H., Wolfram, J., 2007. Measurements of static and dynamic mooring line damping and their importance for floating WEC devices. *Ocean Eng.* 34 (14–15), 1918–1934.
- Lee, S.C., Song, S., Park, S., 2021. Platform motions and mooring system coupled solver for a moored floating platform in a wave. *Processes* 9 (8), 1393.
- Lin, P., Liu, P.L.F., 1998. A numerical study of breaking waves in the surf zone. *J. Fluid Mech.* 359, 239–264.
- Lind, S.J., Rogers, B.D., Stansby, P.K., 2020. Review of smoothed particle hydrodynamics: towards converged Lagrangian flow modelling. *Proceedings of the Royal Society A* 476 (2241), 20190801.
- Liu, Y., Xiao, Q., Incecik, A., Peyrard, C., Wan, D., 2017. Establishing a fully coupled CFD analysis tool for floating offshore wind turbines. *Renewable Energy* 112, 280–301.
- Liu, Z., Wang, Y., 2020. Numerical investigations and optimizations of typical submerged box-type floating breakwaters using SPH. *Ocean Eng.* 209, 107475.
- Luo, M., Khayyer, A., Lin, P., 2021. Particle methods in ocean and coastal engineering. *Appl. Ocean Res.* 114, 102734.
- Lyu, H.G., Sun, P.N., Huang, X.T., Zhong, S.Y., Peng, Y.X., Jiang, T., Ji, C.N., 2022. A Review of SPH Techniques for Hydrodynamic Simulations of Ocean Energy Devices. *Energies* 15 (2), 502.
- Martin, T., Kamath, A., Bihs, H., 2020. Accurate modeling of the interaction of constrained floating structures and complex free surfaces using a new quasistatic mooring model. *Int. J. Numer. Methods Fluids*.
- Masciola, M., Jonkman, J., Robertson, A., 2013. Implementation of a multisegmented, quasi-static cable model. In: *The Twenty-third International Offshore and Polar Engineering Conference*. International Society of Offshore and Polar Engineers.
- Palm, J., Eskilsson, C., Paredes, G.M., Bergdahl, L., 2016. Coupled mooring analysis for floating wave energy converters using CFD: Formulation and validation. *International Journal of Marine Energy* 16, 83–99.
- Palm, J., Eskilsson, C., Bergdahl, L., 2017. An hp-adaptive discontinuous Galerkin method for modelling snap loads in mooring cables. *Ocean Eng.* 144, 266–276.
- Quallen, S., Xing, T., Carrica, P., Li, Y., Xu, J., 2014. CFD simulation of a floating offshore wind turbine system using a quasi-static crowfoot mooring-line model. *Journal of Ocean and Wind Energy* 1 (3), 143–152.
- Rusche, H., 2002. Computational fluid dynamics of dispersed two-phase flows at high phase fractions. Imperial College. PhD thesis.
- Tran, T.T., Kim, D.H., 2016. Fully coupled aero-hydrodynamic analysis of a semi-submersible FOWT using a dynamic fluid body interaction approach. *Renewable Energy* 92, 244–261.
- Tran, T.T., Kim, D.H., 2018. A CFD study of coupled aerodynamic-hydrodynamic loads on a semisubmersible floating offshore wind turbine. *Wind Energy* 21 (1), 70–85.
- Tsai, I.C., Li, S.Y., Hsiao, S.C., Hsiao, Y., 2021. Numerical simulation of 2-D fluid-structure interaction with a tightly coupled solver and establishment of the mooring model. *International Journal of Naval Architecture and Ocean Engineering* 13, 433–449.
- Weller, H.G., Tabor, G., Jasak, H., Fureby, C., 1998. A tensorial approach to computational continuum mechanics using object-oriented techniques. *Computers in Physics* 12 (6), 620–631.
- Windt, C., Davidson, J., Chandar, D.D., Faedo, N., Ringwood, J.V., 2020. Evaluation of the overset grid method for control studies of wave energy converters in OpenFOAM numerical wave tanks. *Journal of Ocean Engineering and Marine Energy* 6 (1), 55–70.
- Wu, M., Stratigaki, V., Troch, P., Altomare, C., Verbrugge, T., Crespo, A., Gómez-Gesteira, M., 2019. Experimental study of a moored floating oscillating water column wave-energy converter and of a moored cubic box. *Energies* 12 (10), 1834.
- Xu, S., Wang, S., Soares, C.G., 2019. Review of mooring design for floating wave energy converters. *Renewable Sustainable Energy Rev.* 111, 595–621.
- Zhang, Y., Kim, B., 2018. A fully coupled computational fluid dynamics method for analysis of semi-submersible floating offshore wind turbines under wind-wave excitation conditions based on OCS data. *Applied Sciences* 8 (11), 2314.